Fe_3C-coated nitrogen-doped CNT/cattail-derived carbon microtube composites for efficient microwave absorption

Huang Fei[1], Wu Peikun[1], Wang Chang[1], Zhang Min[1],
Wang Zhongliao[1], Liu Qiangchun[1,*], Kong Xiangkai[2,*]

(1. *Anhui Province Key Laboratory of Intelligent Computing and Applications*, *Huaibei Normal University*, *Huaibei* 235000, *China*;
2. *School of Materials and Physics*, *China University of Mining and Technology*, *Xuzhou* 221116, *China*)

Abstract: Due to the inherent limited dielectric loss of carbon materials, their attenuation ability and impedance matching are often unsatisfactory. To overcome these problems, hierarchical structures and combined microwave loss mechanisms have attracted considerable attention in the development of high performance microwave absorbers. In this work, biomass cattail was used as a sustainable precursor to synthesize nitrogen-doped carbon nanotube arrays decorated with Fe_3C nanoparticles by chemical vapor deposition. The resulting cattail-derived carbon-based tubular composites (Fe_3C@NCNTs/CMTs) feature a unique Fe_3C-coated, nitrogen-doped carbon nanotube structure. The influence of crystallinity, tuned by calcination at different temperatures, on microwave absorption was investigated. Remarkably, at 800 °C, Fe_3C@NCNTs/CMTs achieved a minimum reflection loss of −35.8 dB and an effective absorption bandwidth of 7.02 GHz at a thickness of only 1.7 mm, even at an ultralow filler loading of 10%, effectively covering the entire Ku band and part of the X band. The excellent microwave absorption performance is attributed to the combined contribution of increased magnetic loss and multiple dielectric polarization mechanisms. This study shows a promising strategy for designing biomass-derived carbon-based broadband microwave absorbing materials.

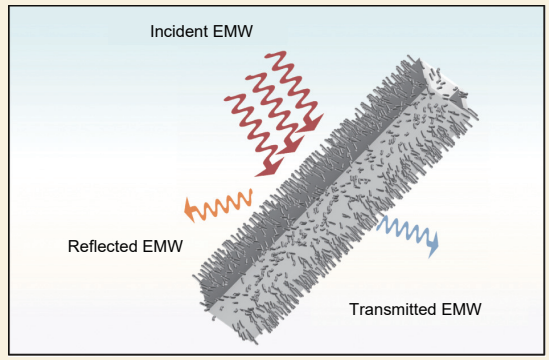

Key words: Hierarchical structure；Electromagnetic synergy；Dielectric loss；Microwave absorption；Carbon microtubes

1 Introduction

With the rapid development of 5G technology and the widespread application of high- frequency electronic and communication equipment, the consequent electromagnetic radiation and interference have seriously affected information security, equipment performance, and human health[1–5]. In recent years, microwave absorbing materials have attracted wide attention from researchers, and some research results have been reported, such as carbon materials[6], graphene[7], carbon nanotubes (CNTs)[8–9], magnetic materials[10], ceramic materials[11], metal-organic framework (MOF)[12], and MXene[13–14]. Carbon-based materials have become promising candidates for high-performance microwave absorption (MA) applications by their chemical stability, low density, and tunable dielectric properties[15]. However, carbon materials still face issues such as impedance mismatch and single loss mechanism[16]. Therefore, the synergistic loss mechanism, which is the MA composite material that interacts with dielectric loss and magnetic loss, has attracted great attention[17–20]. Li et al.[21] prepared BN/Ni/CNT hybrid materials through a carbonization method and fabricated flexible BN/Ni/CNT/WPU films using a knife-coating process. The notable MA performance from dielectric loss, magnetic loss and appropriate impedance matching. Jiang et al.[22] achieved the minimum reflection loss (RL_{min}) of −63.1 dB and the effective absorption bandwidth (EAB) of

Received: August 26, 2025
Revised: November 09, 2025
Accepted: November 10, 2025

7.3 GHz for the Fe/Fe_5C_2@NC-800 material with only 4% filler loading, based on a dual attenuation mechanism involving dielectric and magnetic losses. Li et al.[23] utilized an ice-templated freeze-casting method combined with an annealing process to fabricate a ceramic nanofiber aerogel composed of silica nanofibers, graphene, and metal–organic framework (MOF) derivatives. This approach enabled the efficient integration of MOF-derived magnetic nanoparticles, and the synergistic mechanism between dielectric and magnetic components significantly enhanced the MA performance. Gao et al.[24] prepared Fe/SiC composite materials with core/shell structure through thermal assisted synthesis process, successfully combining dielectric loss material and magnetic loss material together, achieving a RL_{min} of −51 dB at an absorber thickness of 2.01 mm. Wang et al.[25] successfully prepared Fe_3O_4-graphite composite materials by solvothermal method. The optimization of the microwave properties and impedance matching characteristics of the sample is achieved by controlling the proportion of graphite dosage. The magneto electric synergistic loss between Fe_3O_4 nano magnetic particles and graphite significantly improves the MA performance of the material.

In previous reports, well-designed microstructures and adjustable chemical compositions have generated multiple scatterings and construct multi-layer hetero- geneous interfaces. In addition, they have provided conduction loss, dipole polarization, and interface polarization to optimize impedance matching and enhance MA loss capability[26–28]. Jiang et al.[29] synthesized highly efficient multiscale MA materials by chemical blowing and subsequent in-situ growth processes. Benefiting from the advantages in composition and structure, Fe/Fe_3C@NC-2 exhibited exceptional wave-absorption performance exceeding −50 dB across the entire frequency bands (S, C, X and Ku bands). Liu et al.[30] utilized a simple pyrolysis method to prepare a series of graded carbon nanotubes @ Ni/C foam (CNCF). By controlling the loading amount of CNTs, it has a obvious impact on the microwave parameters of CNCFs. When the relative carbon content of the sample is 66.3% and the thickness is 1.8 mm, its EAB reaches 5.8 GHz, and the RL_{min} is −47.0 dB. Di et al.[31] successfully designed Ni/C/porous carbon nanosheet composite materials. The continuous conductive network, numerous defects, and heterogeneous interfaces have promoted the conductivity loss and polarization loss, realized impedance matching, and exhibited positive MA performance. Zhang et al.[32] prepared hollow N-doped carbon polyhedra by embedding CoNi alloy nanoparticles into N-doped graphene using a metal organic framework structure as a template. The hollow N-doped carbon polyhedral structure effectively limits the surface oxidation behavior of CoNi alloy nanoparticles, and owing to the introduction of Ni, it enhances dielectric loss and has better impedance matching characteristics. Wang et al.[33] introduced $Co_3SnC_{0.7}$ multi-component nanoparticles and one-dimensional nanofibers as heterostructure microwave absorbers through electrospinning design. It improves magnetic loss and impedance matching, exhibiting efficient MA performance. The above analysis provides us with reference value and design strategy for the synthesis of high performance microwave absorbing materials. Therefore, the construction of electromagnetic synergistic loss and special hierarchical structures will bring great application prospects for microwave absorbing materials.

At present, the application of biomass-derived carbon materials in MA has been widely studied. Due to their low density, high conductivity, and good chemical stability, they are expected to develop into high-performance microwave absorbers[34–37]. This study is based on the unique hierarchical structure of biomass-derived carbon. Cattail was used as the raw material, and nitrogen-doped carbon nanotube arrays coated with Fe_3C were constructed, successfully preparing of cattail-derived carbon-based Fe_3C-coated nitrogen-doped carbon tubular (NCNT) composites (Fe_3C@NCNTs/CMTs) using a simple one-step chemical vapor deposition strategy. The effect of crystallization levels of the samples at different calcination temperatures on the MA performance was stud-

ied. At 800 °C, the Fe_3C@NCNTs/CMTs exhibited an RL_{min} of −35.8 dB and an EAB of 7.02 GHz (10.98-18.00 GHz) at a thickness of 1.7 mm, demonstrating excellent MA performance. Therefore, this study provides promising strategies for the design of biomass carbon-based materials and broadband absorbers.

2 Experiment

2.1 Materials

Biomass cattail was got from Huaibei, Anhui province, China. $Fe(NO_3)_3·9H_2O$, ethanol, and melamine were bought from Sinopharm Chemical Reagent Co., Ltd. All chemical reagents used are analytical grade and can be used directly.

2.2 Preparation of CMT

Biomass cattails were washed several times with deionized water and ethanol, and then placed in a drying oven at 60 °C for 24 h. The required amount of the biomass cattail was placed in a horizontal tube furnace. Under N_2 atmosphere, it was heated at a rate of 5 °C/min to 800 °C, kept for 2 h, and then naturally cooled to obtain biomass derived carbon micro-tube, named CMT-800.

2.3 Preparation of Fe_3C@NCNTs/CMTs composites

1 g of $Fe(NO_3)_3·9H_2O$ and 150 mg of biomass cattail were dissolved thoroughly in 20 mol L^{-1} of ethanol solution, and stirred continuously at 60 °C for 30 min. After allowing it to stand for 1 h, it was taken out and placed in a fume hood to air dry for 24 h to obtain the sample. The melamine reagent and the required amount of sample were placed at the front and rear positions in the center of inside the horizontal tube furnace. Under nitrogen protection, heating at 5 °C/min, the sample was heated to 800 °C, kept for 2 h, and then naturally cooled. Finally, the Fe_3C@NCNTs/CMTs composite material was obtained, and named FCC-800. In order to research the influence of crystallinity of the samples on the MA performance, they were prepared by changing the calcination temperature, with 700 and 900 °C, during the preparation process, and named FCC-700 and FCC-900, respectively.

2.4 Characterization

The morphology and microstructure were characterized using scanning electron microscope (SEM, Hitachi, SU8220). Transmission electron microscopy (TEM, JEOL JEM-2100) was used to research the morphology of samples. The crystal type was characterized with an X-ray diffraction (XRD) analyzer under Cu $K\alpha$ radiation (λ = 0.154 06 nm) conditions. Raman spectra were obtained with a Raman Spectrometer (Renishaw, reflection mode) with a 532 nm excitation laser. X-ray photoelectron spectroscopy (Thermal Science, ESCALAB 250Xi) was acquired to analyze the elemental composition and chemical states of the composite materials, using an X-ray source with a wavelength of 0.834 nm. Magnetic properties were measured at room temperature using a vibrating sample magnetometer (VSM; Lakeshore 7404/8604).

2.5 Microwave absorbing measurement

The Vector Network Analyzer (VNA, AV3629D) was used to test the electro- magnetic parameters of samples at frequencies ranging from 2 to 18 GHz. The test samples were prepared by uniformly mixing the sample with paraffin in a mass ratio of 1∶9. Then, the obtained mixtures were put in a mold, respectively, to form coaxial ring test complex under compaction. Based on the measurement data, the reflection loss values of samples with a thickness of 1–5 mm were calculated using transmission line theory at 2–18 GHz.

2.6 CST simulation

Under actual far-field simulation conditions, CST Studio Suite 2021 was employed to calculate and analyze the electric field intensity distribution, power loss density, and radar cross section (RCS) of the sample. The RCS was computed using the following Eq. (1):

$$\sigma(dBm^2) = 10\log\left(\frac{4\pi S}{\lambda^2}\left|\frac{E_S}{E_i}\right|^2\right) \quad (1)$$

where S denotes the simulation region, λ stands for the wavelength of the incident wave, and E_s and E_i represent the scattered electric field intensity and incident electric field intensity, respectively. The RCS simulation model comprises a 1.0 mm-thick ideal electrical

conductor (PEC) plate at the bottom and a 1.55 mm-thick absorber/paraffin composite layer (10%) at the top. The 200 mm × 200 mm double-layer model was placed on the X-O-Y plane, with the plane wave incident along the negative Z-axis direction. Open boundary conditions were applied to the electromagnetic wave (EMW) incident direction, while periodic boundary conditions were set for the other directions. The monitoring frequency was set to 17.76 GHz, and the incident wave's azimuth angle was configured as $-90° \leqslant \theta \leqslant 90°$ with $\varphi = 90°$.

3 Results and discussion

3.1 Microstructure and the chemical composition

Fig. 1 shows SEM and TEM images of the CMT-800 and composites. The CMT-800 exhibits a one-dimensional (1D) tubular structure (Fig. 1a), and CNTs adhere to the surface of CMTs in composites (Fig. 1b-d). Specifically, CNTs grow on the surface of the CMT at 700 °C. When the calcination temperature rises to 800 °C, it is evident that CNTs interact with each other and grow on the surface of the CMT, with smaller sizes and larger morphological differences. When the temperature reaches 900 °C, CNTs aggregate on the surface of the CMT and cluster forms. Furthermore, from the TEM image of FCC-800 in Fig. 1e, Fe_3C nanoparticles were mainly observed at the tips of the CNTs, with a size of approximately 100 nm. This phenomenon can be attributed to the limited internal space of the nanotubes, which makes Fe_3C more easily encapsulated at the tips, resulting in tip enrichment as revealed in the TEM images. Specifically, as shown in Fig. 1f, the thickness of the graphitized carbon layer is about 7.5 nm, and many defects are discovered in the graphite carbon, which maybe the reason of N atom doping replacing C atoms. The nanoparticles with a lattice spacing of 0.203 nm encapsulated in CNTs can be attributed to the (220) crystal plane of Fe_3C (Fig. 1g)[38]. To explain this phenomenon, melamine is considered to serve dual functions during high-temperature calcination: (1) as a carbon and N source, and (2) facilitating the reduction of Fe ions into Fe_3C nanoparticles. These Fe_3C nanoparticles subsequently catalyze the growth of N-doped C nanotube (Fe_3C@NCNT). Compared with CMT, the resulting structure establishes enhanced conductive networks among carbon nanotubes. This optimized architecture promotes polarization and interaction between magnetic nanoparticles, enabling efficient energy conversion between magnetic permeability and dielectric constant, thereby improving dielectric loss capabilities[39].

Fig. 2a and Fig. S2 display the XRD pattern of the sample, where the diffraction peaks observed at 2θ=21.6° and 26.1° can be attributed to the (120) and (002) crystal planes of graphitic carbon (PDF#41-1487)[40]. Notably, the (002) diffraction peaks of FCC-800 and FCC-900 exhibit pronounced intensity, which is ascribed to the formation of graphitic carbon derived from carbon nanotubes (CNTs)[41–42]. In addition,

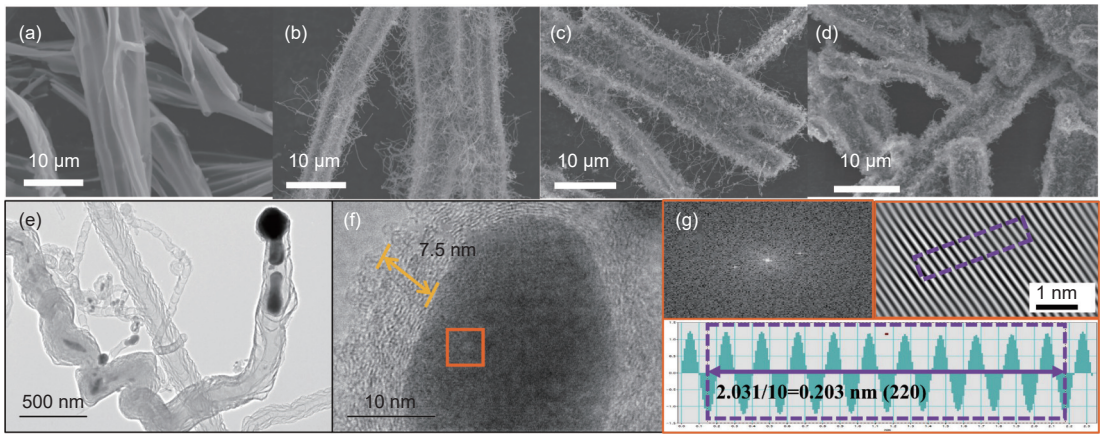

Fig. 1 SEM images of (a) CMT-800, (b) FCC-700; (c) FCC-800 and (d) FCC-900. (e) TEM image of FCC-800. (f, g) HRTEM image of FCC-800 with SAED mode

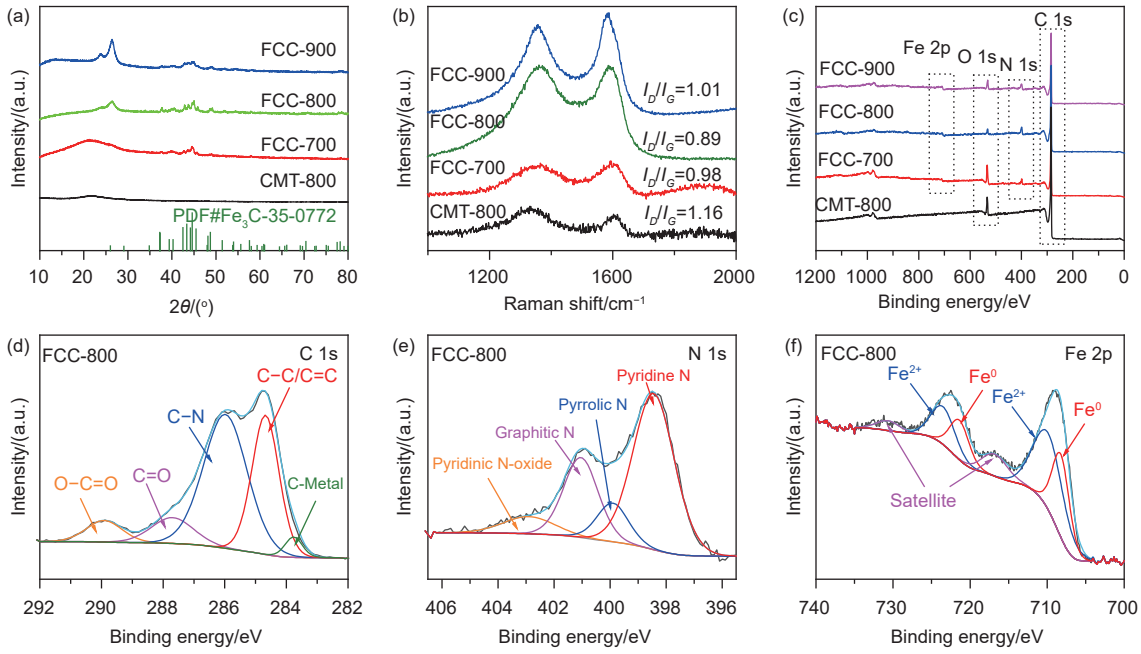

Fig. 2 (a) XRD patterns and (b) Raman spectra of all samples. (c) XPS spectra of FCC-800 and high-resolution XPS spectra of (e) C 1s, (f) N 1s and (d) Fe 2p

it can be observed that the diffraction peaks of the composite material in the range of 30°–60° highly match Fe_3C (PDF#: 35-0772), indicating that during high-temperature annealing, iron salts react with carbon to ultimately form Fe_3C. Through comparative analysis of spectral data, it was observed that with the continuous increase of calcination temperature, the intensity of the (002) diffraction peak gradually intensified, indicating enhanced graphitization degree. The presence of graphitic carbon increased the electrical conductivity of the composite material, thereby promoting higher conductive loss of electromagnetic waves through improved electrical pathways. It is worthy of remark that the diffraction peak of Fe_3C in FCC-800 is the most obvious, and the shape of the peak tends to be sharp, indicating that the growth and nucleation of Fe_3C nanoparticles are most favorable at 800 °C.

Raman spectroscopy is used to further investigate the degree of graphitization and defects in carbon materials. The peaks near 1341 and 1590 cm^{-1} correspond to the *D* band (indicating defects in the carbon atomic lattice) and the *G* band (indicating the degree of graphitization of the carbon material), respectively (Fig. 2b)[43]. The ratio of I_D/I_G is used to reflect the degree of graphitization or defect in carbon materials[44]. The I_D/I_G ratios of CMT-800, FCC-700, FCC-800 and FCC-900 correspond to 1.16, 0.98, 0.89 and 1.01, respectively. From the above data comparison, the graphitization degree of CMT-800 is relatively lower, while for composites, the addition of CNT enhances its graphitization degree, which accords with the XRD characterization results. Notably, when the annealing temperature reaches 800 °C, FCC-800 exhibits the smallest I_D/I_G ratio, indicating the highest degree of graphitization. The graphitization degree is positively correlated with electrical conductivity. Enhanced electrical conductivity improves the dielectric loss of the electromagnetic wave absorber, making a higher graphitization level beneficial for electromagnetic wave attenuation. Under the action of an electromagnetic field, defect sites act as polarization centers and strengthen dipole polarization, which facilitates the dissipation of EMW energy.

The elemental composition and valence states of elements in the CMT-800 and FCC-*x* were examined by XPS. Fig. 2c shows signal peaks for Fe, O, C and N elements on the full spectrum. The C 1s XPS spectrum is divided into 5 peaks around 283.8, 284.7, 285.9, 287.8 and 289.8 eV, proving the existence of

C—Fe, C—C/C=C, C—N, C=O and O—C=O bonds, respectively (Fig. 2d). The peak at 283.8 eV corresponds to the Fe—C bond, further confirming the presence of Fe_3C[45]. The peaks observed in the N 1s spectrum at 398.4, 399.9, 401.0 and 402.8 eV belong to pyridine N, pyrrole N, graphite N and oxidized N—O, respectively (Fig. 2e)[46]. The Fe 2p high-resolution spectrum of FCC-800 was investigated in Fig. 2f, where the peaks at 708.2 and 721.5 eV are regarded as the metallic Fe (Fe^0), the peaks at 709.8 and 723.9 eV are consistent with Fe^{2+}, and the peaks at 716.8 and 730.9 eV are considered to satellite peaks, respectively[47]. The above results successfully confirmed the existence of N doping in the sample of FCC-800. Due to the presence of these N-doped CNTs and Fe_3C, multi-layer heterogeneous interfaces are constructed, and the magneto electric synergistic effect improves dipole polarization and magnetic loss. At the same time, graphite N is beneficial for conduction loss[48].

The BET specific surface areas of CMT-800 and FCC composite materials were characterized by N_2 adsorption-desorption tests. The Type IV isothermal profiles (Fig. S3) were observed across all specimens, evidencing the co-existence of microporous and mesoporous structures within the materials. Derived from biomass, CMT-800 possesses an ultra-high specific surface area (432.49 $m^2\ g^{-1}$) and a small pore size (4.69 nm). However, due to the excessively high ε_r and the lack of magnetic properties, severe impedance mismatch still occurs. The specific surface areas and pore sizes of FCC-700, FCC-800 and FCC-900 are 12.31 $m^2\ g^{-1}$ and 19.49 nm, 63.19 $m^2\ g^{-1}$ and 13.46 nm, and 57.71 $m^2\ g^{-1}$ and 8.17 nm, respectively. SEM observations reveal that NCNTs grow sparsely in some cases (FCC-700), while Fe_3C tends to agglomerate (FCC-900). In contrast, FCC-800 exhibits denser and more uniform growth of NCNTs, along with well-dispersed Fe_3C particles without significant agglomeration or structural densification. As a result, FCC-800 demonstrates the largest specific surface area among the FCC series, along with a moderate pore size. The distinctive architecture establishes multiple interfacial polarization domains, enabling superior electromagnetic energy attenuation through optimized dielectric loss mechanisms[49].

3.2 Electromagnetic parameter analysis and MA performance

The MA characteristics are generally closely related to the electromagnetic parameters. The relative complex permittivity ($\varepsilon_r=\varepsilon' -j\varepsilon''$) and permeability ($\mu_r=\mu'-j\mu''$) are used to evaluate microwave performance[50]. Adjusting electromagnetic parameters enables balancing between ε_r and μ_r, where the real components (ε', μ') govern electricmagnetic energy storage, and the imaginary components (ε'', μ'') relate to electricmagnetic energy dissipation. Usually, the dielectric and magnetic loss capabilities of microwave absorbers are evaluated using the dielectric loss tangent ($tg\delta_\varepsilon=\varepsilon''/\varepsilon'$) and the magnetic loss tangent ($tg\delta_\mu=\mu''/\mu'$), respectively. The electromagnetic parameters of the four samples are shown in Fig. 3. It can be seen that the values of ε' and ε'' show a decreasing trend in the frequency range of 2–18 GHz, which can be attributed to the dispersion behavior of the sample. This phenomenon is beneficial for improving the MA efficiency of composite materials[51]. As shown in Fig. 3a-b, with the increase of frequency, ε' and ε'' values of the CMT-800 range from 23.2 to 11.4 and 20.2 to 7.5 respectively, which is significantly higher than that of FCC-700 (12.3-8.8, 3.6-3.3), FCC-800 (19.6-6.5, 7.4-3.5), and FCC-900 (22.4-10.2, 13.7-7.7). This demonstrates that the CMT contains superior electrical energy storage and wave dissipation capabilities. To further evaluate the microwave loss capability of the samples, the dielectric loss tangent ($tg\delta_\varepsilon$) was calculated in Fig. 3c. CMT-800 exhibits a higher $tg\delta_\varepsilon$ value, while those of FCC-800 and FCC-900 are relatively close, indicating that CMT-800 possesses stronger dielectric loss capability with FCC-800 and FCC-900 following in order. However, the excessively high $tg\delta_\varepsilon$ value may also lead to impedance mismatch of the material, which is precisely why CMT exhibits poor MA performance. Additionally, magnetic loss constitutes a significant component of the microwave attenuation mechanism. Due to the magnetic loss caused

by magnetic nanoparticles, the magnetic properties of the material were initially tested using a vibrating sample magnetometer. As shown in Fig. 3d-e, the saturation magnetization strengths of FCC-700, FCC-800 and FCC-900 are 23.8, 21.2 and 12.5 emu/g, respectively. By comparison, it can be seen that as the calcination temperature increases, the values of FCC-700 and FCC-800 are high, while the values of FCC-900 are low. This phenomenon indicates the influence of calcination temperature on the growth of Fe_3C nanoparticles. Under suitable temperature conditions, it is beneficial for the growth of Fe_3C. However, an excessively high calcination temperature may promote the tendency of magnetic particles to aggregate, which could in turn influence the exchange coupling between them[52]. Furthermore, it can be clearly seen from Fig. 3e that FCC-800 has a significant coercivity (H_c). Overall, a higher Ms can generate a stronger macroscopic magnetic moment, thereby facilitating enhanced electromagnetic wave absorption[53]. With lower intrinsic coercivity, this characteristic is conducive to improving the initial permeability, thereby enhancing the magnetic loss capacity[54]. For CMT-800, FCC-700, FCC-800 and FCC-900, their μ' values are close to 1.2. Meanwhile, the μ'' of CMT-800 is almost zero across the entire test frequency range (2 GHz–18 GHz) due to its non-magnetic characteristic. However, as observed from the figure, the μ'' of FCC-700, FCC-800 and FCC-900 exhibit higher values than CMT-800, which can be owed to the introduction of mag-

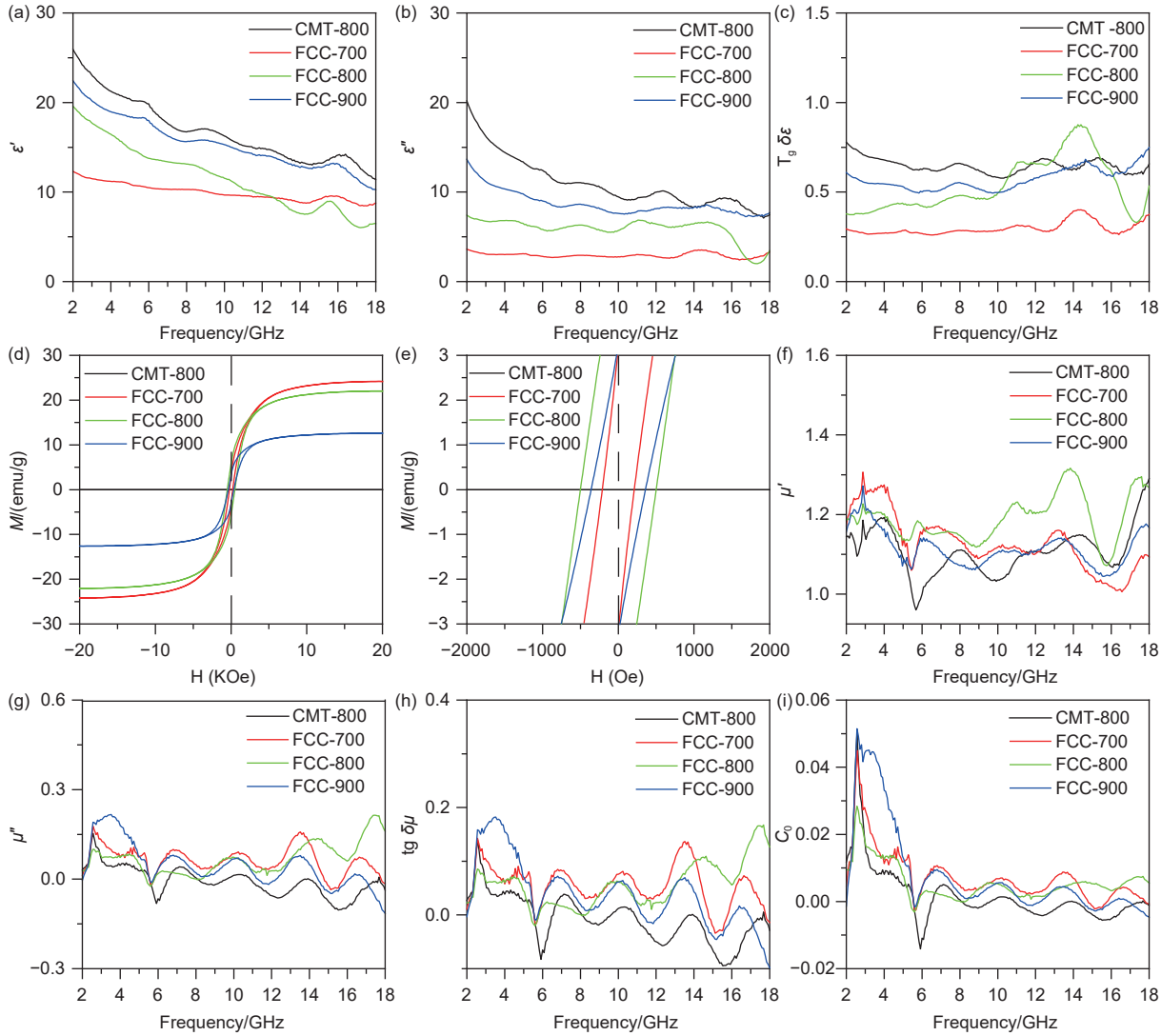

Fig. 3 (a) ε', (b) ε'', (c) $T_g\ \delta\varepsilon$, (d-e) the magnetization hysteresis loops, (f) μ', (g) μ'', (h) tg $\delta\mu$ and (i) C_0 curves of CMT-800, FCC-700, FCC-800 and FCC-900

netic Fe_3C particles. This observation is consistent with the results obtained from the M-H curve measurements (Fig. 3f-g). These weak magnetic loss capabilities may be due to the ultra-low filler loading of absorber. Besides, μ'' has negative values when the induced magnetic field from charge carrier motion exceeds the applied field. Meanwhile, as the composite's conductivity approaches the percolation threshold, the skin effect becomes dominant, shielding against microwave penetration and thereby reducing permeability[55].

It is widely believed that magnetic losses come from natural resonance, exchange resonance, and eddy current losses in the range of 2–18 GHz[56]. Usually, the eddy current coefficient C_0 ($C_0 = \mu''(\mu')^{-2}f^{-1}$) is used to determine the type of magnetic loss. When magnetism is only generated by eddy current losses, the value of C_0 remains constant. As shown in Fig. 3i, C_0 fluctuates within the tested frequency range, indicating that magnetic losses are mainly caused by natural resonance and exchange resonance, while eddy current losses are not the main factor. In addition, the magnetic loss coefficient is lower than the dielectric loss coefficient, indicating that the attenuation of microwaves is mainly determined by dielectric loss (Fig. 3h).

There are multiple resonance peaks in the ε'' curves of all samples, indicating the presence of multipolar relaxation processes. According to the Debye relaxation theory[57–58], the relationship between ε' and ε'' is expressed as Eq. (2):

$$[\varepsilon' - (\varepsilon_s + \varepsilon_\infty)/2]^2 + [\varepsilon'']^2 = \left[\frac{\varepsilon_s + \varepsilon_\infty}{2}\right]^2 \quad (2)$$

where ε_s and ε_∞ are the static permittivity and relative permittivity at the high-frequency limit, respectively. The semicircles in the ε' and ε'' curves are called Cole-Cole semicircles, each representing a Debye dipole relaxation process[59]. From Fig. 4, it can be seen that among all the samples, the Fe_3C@NCNTs/CMTs composite demonstrates enhanced Cole-Cole semicircle characteristics relative to CMT-800, which is due to the interface polarization generated by the hierarchical structure of the sample and the defect polarization caused by a large number of defects generated by nitrogen doping. Additionally, CMT-800 and FCC-900 exhibit longer trails, leading to excessive conductivity loss, while FCC-700, with a shorter trail, results in insufficient conductivity loss[60]. Compared to the other samples, FCC-800 demonstrates superior polarization and conductivity losses.

RL is used to characterize the microwave absorption performance of materials. The coaxial method is used to measure the relative complex permittivity (ε_r) and complex conductivity (μ_r), and *RL* is evaluated through transmission line theory[61]. The calculation formula is represented by Eq. (3) and (4):

$$RL = 20\log|(Z_{in} - Z_o)/(Z_{in} + Z_o)| \quad (3)$$

$$Z_{in} = Z_o\sqrt{\frac{\mu_r}{\varepsilon_r}}\tan h\left[j\frac{2\pi f d}{c}\sqrt{\mu_r\varepsilon_r}\right] \quad (4)$$

where Z_{in} is the input impedance matching, and Z_o is the free space impedance matching, c is the speed of light, d is the thickness of medium, f is frequency, ε_r and μ_r are the relative complex permittivity and the relative complex permeability. Generally, when the *RL* value falls below −10 dB, the microwave absorber can effectively attenuate 90% of microwave. The goal of researching new microwave absorbing composite materials is to achieve high absorption strength and ultra wide EAB.

Fig. 5 shows the dependence of the *RL* values on frequency of the CMT-800 and the Fe_3C@NCNTs/CMTs at different mating thicknesses. Overall, compared with the CMT, the composites exhibit better MA performance due to their reasonable hierarchical structure and electromagnetic synergistic effect. Specifically, at a thickness of 1.7 mm, the CMT-800 can only achieve an RL_{min} of −11.30 dB at 11.2 GHz and an EAB of 1.62 GHz, while demonstrating an EAB_{max} of 3.2 GHz (11.28–14.48 GHz) at the optimal matching thickness of 1.5 mm (Fig. 5a-c). The FCC-700 exhibits an outstanding RL_{min} of −25.1 dB and an EAB_{max} of 5.04 GHz (12.56–17.60 GHz) at a matching thickness of 1.7 mm (Fig. 5d-f). At a matching thickness of 1.7 mm, FCC-800 exhibits the RL_{min} reaching −35.8 dB, and achieves an EAB_{max} of 7.02 GHz within the 10.98 GHz-18.00 GHz frequency range, fully covering the entire Ku band and a portion of the X

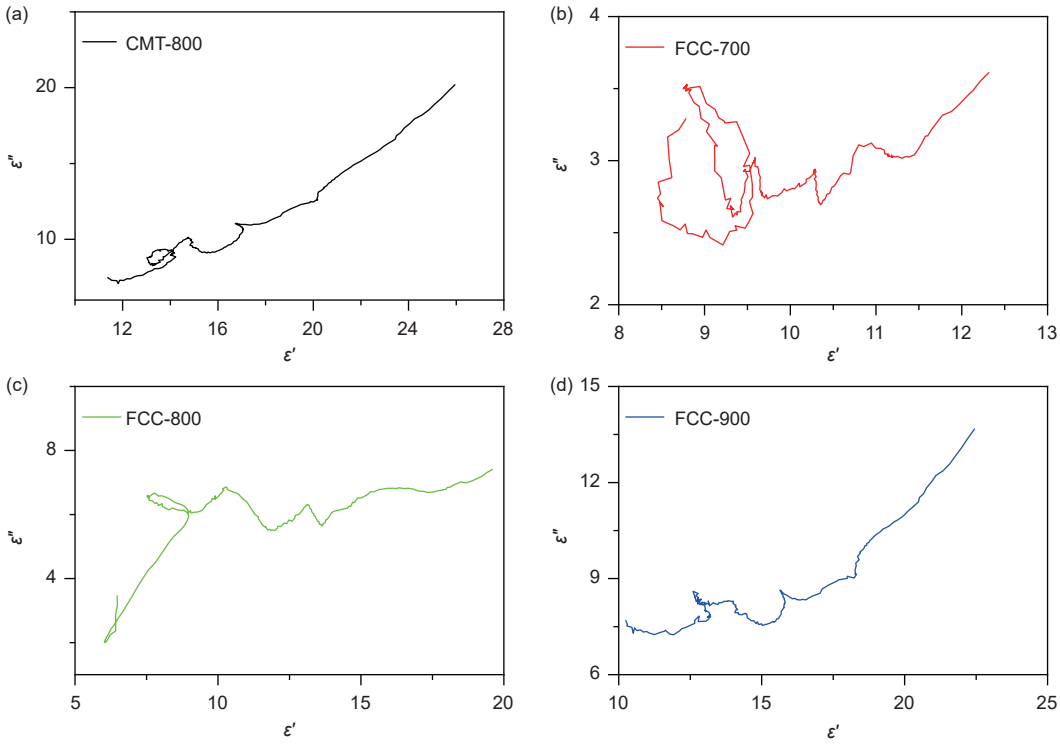

Fig. 4 Cole-Cole curves for (a) CMT-800, (b) FCC-700, (c) FCC-800, and (d) FCC-900

band (Fig. 5g-i). FCC-900 possesses an RL_{min} of −13.2 dB and an EAB_{max} of 2.72 GHz (9.76–12.48 GHz) at a matching thickness of 1.7 mm (Fig. 5j-l). Compared to CMT-800, the Fe_3C@NCNTs/CMTS composite sample exhibits superior microwave absorption performance. The resultant structure establishes an enhanced conductive network between carbon nanotubes. The FCC-*x*-derived structure establishes an enhanced conductive network between carbon nanotubes compared to CMT-800. This optimized architecture promotes polarization and interactions among magnetic nanoparticles, enabling efficient energy conversion between magnetic permeability and dielectric constant, thereby achieving superior MA performance.

When the reflected wave at the absorber–air interface and the reflected wave at the absorber–metal interface have a phase difference of 180°, the EMW is interfered with and attenuated[62]. Based on the quarter-wavelength matching model, the relationship between the peak reflection loss frequency (f_m) and the corresponding thickness (t_m) can be explained. This phenomenon can be explained by the quarter-wavelength cancellation model, which is represented as[63] Eq. (5):

$$t_m = \frac{n\lambda}{4} = \frac{nc}{4f_m\sqrt{|\mu_r||\varepsilon_r|}}(n = 1,3,5\cdots) \quad (5)$$

where t_m is the matching thickness, λ is the wavelength at a specific frequency, and f_m is the matching frequency. As shown in Fig. S4(a-d), the experimental data of sample CMT-800, FCC-700, FCC-800 and FCC-900 exhibit good agreement with the theoretical prediction, confirming that its microwave attenuation behavior conforms well to the quarter-wavelength model. Additionally, as the matching thickness varies between 1.0–5.0 mm, the peak of the minimum reflection loss (RL_{min}) values shifts toward lower frequencies[64].

To comprehensively evaluate the absorption performance of the absorber, two key factors were further investigated. One is the attenuation capability, which is characterized by the attenuation constant (α), derived from the following Eq. (6)[65].

$$\alpha = \frac{\sqrt{2}}{c}\pi f \times \sqrt{(\mu''\varepsilon'' - \mu'\varepsilon') + \sqrt{(\mu''\varepsilon'' - \mu'\varepsilon')^2 + (\mu'\varepsilon'' + \mu''\varepsilon')^2}} \quad (6)$$

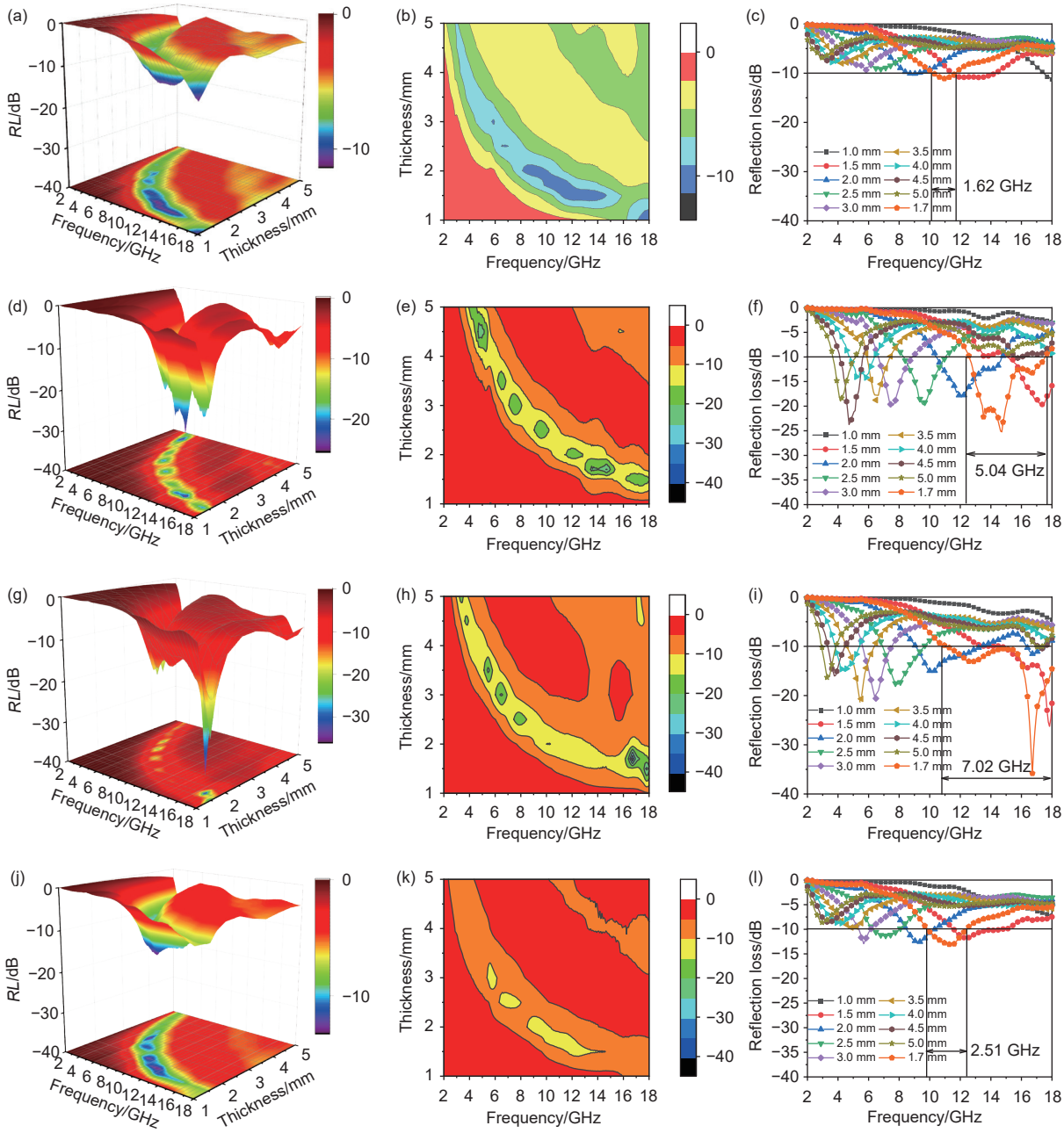

Fig. 5 3D contour and 2D MA performance maps of (a-c) CMT-800, (d-f) FCC-700, (g-i) FCC-800 and (j-l) FCC-900

The higher value of α is related to the dissipation capacity of microwave, and the higher the value of α, the stronger the dissipation capacity of microwave. Fig. 6a displays the variation trend of attenuation constant and frequency of samples material, which increases with the increase of frequency. In the frequency range of 2–18 GHz, while the CMT-800 and FCC-900 samples exhibit higher attenuation constant values (theoretically indicating stronger microwave attenuation capability), the observed *RL* values show inconsistency with this expectation. The excellent MA performance is owed to well-matched impedance, which effectively promotes incident microwaves to penetrate and propagate within the absorber. The impedance Z can be described as $Z=Z_{in}/Z_0$, where Z_{in} is the input impedance of the absorber and Z_0 is the characteristic impedance of free space. That is to say, the closer the Z value is to 1, the better the impedance matching. A good impedance matching is usually considered between 0.8 and 1.2. As shown in Fig. 6b, it is difficult for the Z of the CMT-800 to reach 0.8 at all thicknesses, indicating poor impedance matching.

Fig. 6c-e show that as the calcination temperature arises, the curves of FCC-700 and FCC-800 approach 1, showing good impedance matching. However, a pronounced impedance mismatch is observed in FCC-900, possibly resulting from the inadequate coordination between its permittivity and permeability. Thus, FCC-800 exhibits the excellent MA performance.

Table 1 presents a comparative analysis of FCC-800 with previously reported biomass-derived carbon-based absorbers. Results show that sample FCC-800 offers key benefits such as thinner matching thickness, a wider absorption bandwidth, and reduced filler content. These characteristics highlight its great potential for practical applications in microwave absorption.

CST Studio Suite was employed to further investigate the electromagnetic energy dissipation behavior of Fe_3C@NCNTs/CMTs under practical far-field conditions. Radar cross-section (RCS) simulations were performed to evaluate the practical MA performance of the Fe_3C@NCNTs/CMTs composites. The simulation model consisted of a perfect electric conductor (PEC) plate coated with the target absorbers (Fig. 7a). The three-dimensional (3D) RCS distribution patterns (Fig. 7b-e) reveal that FCC-700, FCC-800 and FCC-900 all exhibit low radar reflection signal intensity. Notably, FCC-800 demonstrates the smallest RCS values, maintaining levels below −10 dB m^2 across a broad scattering angle range from −90° to 90° (Fig. 7f). Remarkably, this material achieves its minimum *RCS* value of −37.01 dBm^2 at 27°, providing compelling evidence of its exceptional practical MA performance[71].

Elucidating the microscopic loss mechanisms is essential for understanding the performance of microwave absorbers (Fig. 7g). The 1D tubular architectures of CNT and CMT facilitate EMW scattering. Multiple scattering predominantly takes place within these 1D tubular structures as well as the 3D conduct-

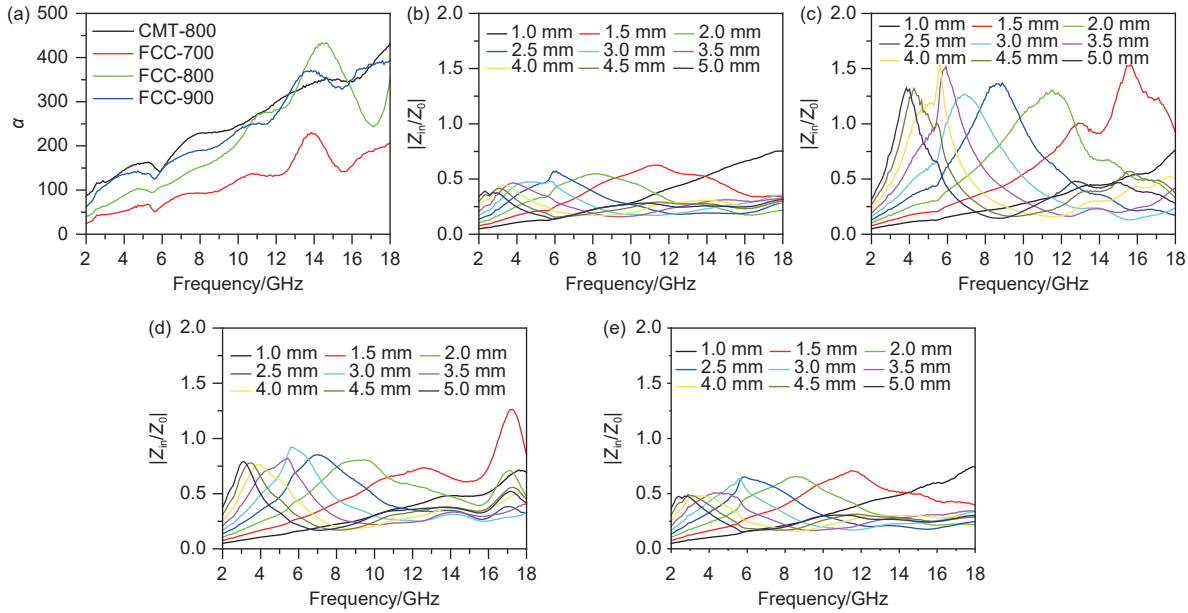

Fig. 6 (a) Attenuation constants (α) and impedance matching curves of (b) CMT-800, (c) FCC-700, (d) FCC-800 and (e) FCC-900

Table 1 Comparison of microwave absorption performance of various biomass-derived carbon- based materials and the present work

Sample	Matrix	Filler loading (%)	RL_{min}/dB	d_m/mm	*EAB*/GHz	Ref.
BC/CoFe	Paraffin	10	−54.4	2.2	2.6 (2.4 mm)	[66]
BPC	Paraffin	30	−53.9	3.03	6.6 (2.0 mm)	[67]
watermelon-derived SC-X	Paraffin	30	−58.7	1.7	3.5	[68]
BPC/Co/CNTs	Paraffin	10	−78.7	1.7	3.5 (3.1 mm)	[69]
BHPC	Paraffin	10	−47.5	2.8	3.4	[70]
FCC-800	Paraffin	10	−35.8	1.7	7.02	This work

Note: BC: Biomass-derived carbon; BPC: Biomass-derived porous carbon; SC: Spherical carbon; BHPC: Biomass hierarchical porous carbon

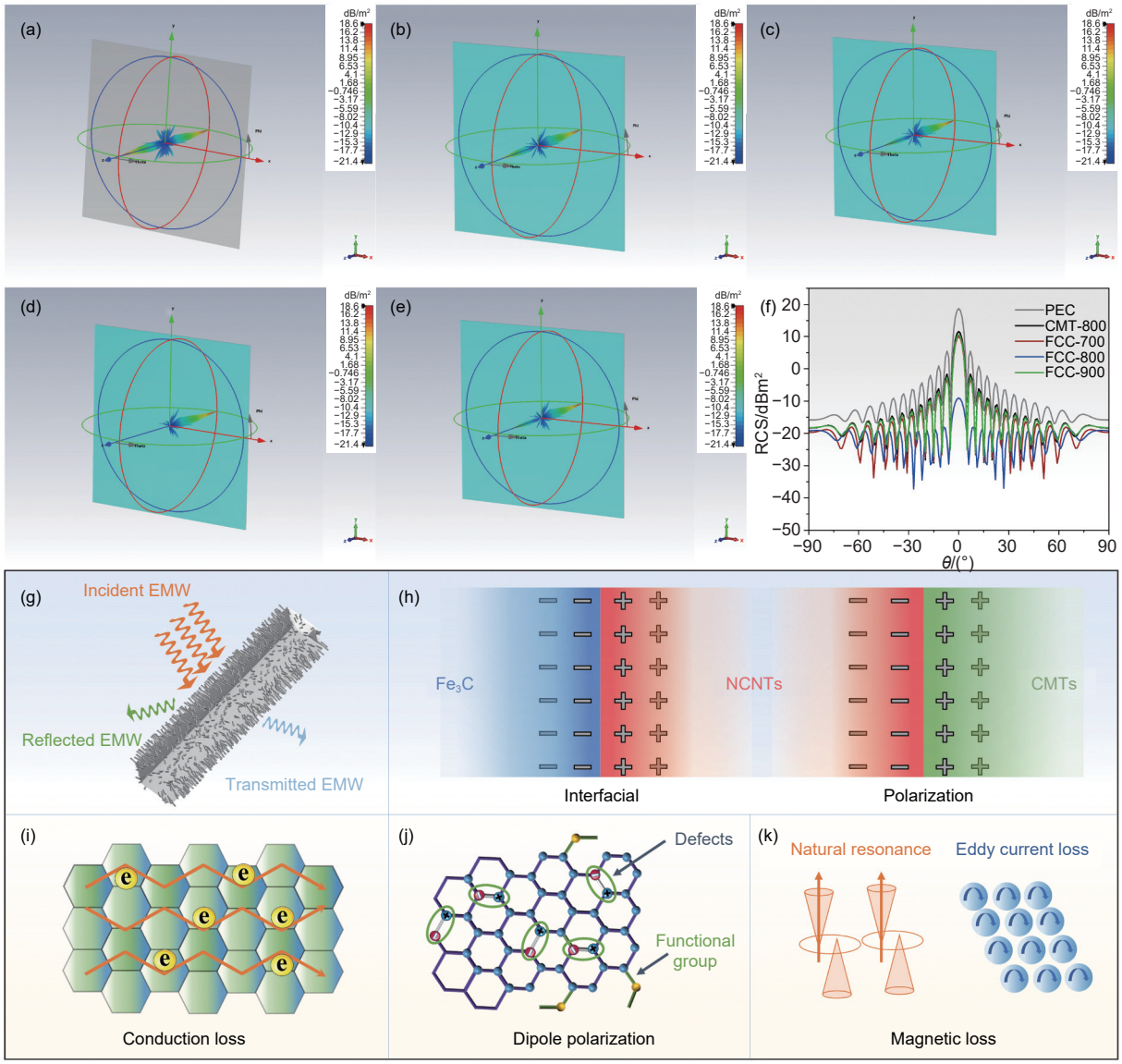

Fig. 7 (a) 3D RCS distribution of PEC conductor, (b) CMT-800, (c) FCC-700, (d) FCC-800 and (e) FCC-900. (f) 2D RCS distribution in 90° and 90° scattering angle regions. (g) Schematic diagram of electromagnetic wave absorption mechanism. (h) Interface polarization. (i) Conductance loss. (j) Dipole polarization. (k) Magnetic loss mechanism

ive network formed by the interweaving of CNT and CMT. The high aspect ratio of CNT offers abundant attachment sites for multiple scattering there by prolonging the propagation path of EMWs (Fig. 7g)[72]. As illustrated in Fig. 7h, local electromagnetic field enhancement regions are generated at the interfaces of Fe_3C/NCNTs and NCNTs/CMTs. These regions strengthen polarization through charge accumulation and dipole rearrangement, thus augmenting interfacial polarization loss. This effect is especially pronounced under high-frequency EMW irradiation[73]. Simultaneously, the migration and hopping of free electrons within Fe_3C, CMTs and N-doped CNTs generated by chemical vapor deposition and catalytic processes contribute significantly to conductive loss (Fig. 7i)[74–75]. Furthermore, pyridinic and pyrrolic N species introduced by N doping can excite dipole polarization under an external electric field (Fig. 7j)[76]. Finally, the Fe_3C component obtained through high-temperature calcination provides magnetic loss (Fig. 7k). The synergistic interplay of these mechanisms with interfacial polarization, conductive loss, dipole polarization, and magnetic loss collectively enhances the MA capacity of the composite material.

4 Conclusion

In summary, this study successfully synthesized nitrogen-doped carbon nanotube arrays coated with Fe_3C using biomass-derived cattail as the raw material through chemical vapor deposition, resulting in the preparation of Fe_3C@NCNTs/CMTs. The influence of crystallinity at various calcination temperatures on the MA performance was investigated. The FCC-800 sample achieved a RL_{min} of −35.8 dB and a broad EAB of 7.02 GHz at a thickness of only 1.7 mm. The excellent MA performance is attributed to the unique hierarchical structure and the synergy between dielectric and magnetic losses, which optimize impedance matching and enhance microwave attenuation. Therefore, the Fe_3C@NCNTs/CMTs offer several advantages, including outstanding RL, wide EAB, thin thickness, light weight, sustainability and ease of preparation. These properties make them a promising candidate for advanced microwave absorbers in the field of MA.

Conflicts of interest

The authors declare that they have no known competing financial interests or personal relationships that could have appeared to influence the work reported in this paper.

Acknowledgements

This work was supported by the Natural Science Foundation of China (21975283, 22279162).

References

[1] Liang C B, Gu Z J, Zhang Y L, et al. Structural design strategies of polymer matrix composites for electromagnetic interference shielding: A Review[J]. Nano-micro Letters, 2021, 13: 181.

[2] Li B, Wang F L, Wang K J, et al. Metal sulfides based composites as promising efficient microwave absorption materials: A review[J]. Journal of Materials Science & Technology, 2022, 104: 244-268.

[3] Lan D, Li H F, Wang M, et al. Recent advances in construction strategies and multifunctional properties of flexible electromagnetic wave absorbing materials[J]. Materials Research Bulletin, 2024, 171: 112630.

[4] Zheng F, Wu P, Wang L, et al. Activated graphite with richly oxygenated surface from spent lithium-ion batteries for microwave absorption[J]. Small, 2025, 21: 2409454.

[5] Kong X, Wu P, Tian S, et al. All-in-one: Multi-parameter engineering on γ-Fe_2O_3 for ultra-broadband microwave absorption[J]. Chemical Engineering Journal, 2024, 485: 150144.

[6] Wu J Z, Zhao Y H, Zhao X Y, et al. Core-shell nanowires comprising silver@polypyrrole-derived pyrolytic carbon for high-efficiency microwave absorption[J]. Journal of Materials Science, 2022, 57: 20672-20684.

[7] Wang P, Yang P L, Ling J C, et al. Frontal ring-opening metathesis polymerized polydicyclopentadiene carbon nanotube/graphene aerogel composites with enhanced electromagnetic interference shielding[J]. Advanced Composites and Hybrid Materials, 2022, 5: 2066-2077.

[8] Xu X, Yao F, Ali O, et al. Adjustable core-sheath architecture of polyaniline-decorated hollow carbon nanofiber nanocomposites with negative permittivity for superb electromagnetic interference shielding[J]. Advanced Composites and Hybrid Materials, 2022, 5: 2002-2011.

[9] Wei M, Wu N, Li B, et al. From MXene to multimodal-responsive smart, durable electromagnetic interference shielding textiles[J]. Advanced Functional Materials, 2025, 35: 2424312.

[10] Kong M Y, Liu X H, Jia Z R, et al. Porous magnetic carbon CoFe alloys@ZnO@C composites based on Zn/Co-based bimetallic MOF with efficient electromagnetic wave absorption[J]. Journal of Colloid and Interface Science, 2021, 604: 39-51.

[11] Wang S, Gong H, Zhang Y, et al. Microwave absorption properties of polymer-derived SiCN(CNTs) composite ceramics[J]. Ceramics International, 2021, 47: 1294-1302.

[12] Zhang X, Tian X L, Wu N, et al. Metal-organic frameworks with fine-tuned interlayer spacing for microwave absorption[J]. Science Advances, 2024, 10: eadl6498.

[13] Song Q, Ye F, Kong L, et al. Graphene and MXene nanomaterials: toward high-performance electromagnetic wave absorption in gigahertz band range[J]. Advanced Functional Materials, 2020, 30: 2000475.

[14] Wu N, Yang Y F, Wang C X, et al. Ultrathin cellulose nanofiber assisted ambient-pressure-dried, ultralight, mechanically robust, multifunctional MXene aerogels[J]. Advanced materials, 2023, 35: 2207969.

[15] Li Z X, Yang W, Zhang C, et al. Multiscale structural design of heterostructured carbon/boron nitride aerogels for efficient thermal conductivity and broadband electromagnetic wave absorption[J]. Chemical Engineering Journal, 2025, 519: 165470.

[16] Li Z X, Wu X, Jiang B, et al. A review of high thermal conductivity carbon-based materials for microwave absorption materials[J]. New Carbon Materials, 2025, 40: 111-130.

[17] Deng B W, Xiang Z, Xiong Z J, et al. Sandwich-like Fe&TiO_2@C nanocomposites derived from MXene/Fe-MOFs hybrids for electromagnetic absorption[J]. Nano-micro Letters, 2020, 12: 55.

[18] Cheng R R, Wang Y, Di X C, et al. Construction of MOF-derived plum-like NiCo@C composite with enhanced multi-polarization for high-efficiency microwave absorption[J]. Journal of Colloid and Interface Science, 2022, 609: 224-234.

[19] Wang C, Kong X, Wang L, et al. Mechanistically engineered heterojunction from spent LFP for efficient oxygen evolution electrocatalysis[J]. Angewandte Chemie International Edition, 2025, 65: e202516122.

[20] Wang X Y, Xing X F, Zhu H S, et al. State of the art and prospects of Fe_3O_4/carbon microwave absorbing composites from the dimension and structure Perspective[J]. Advances in Colloid and Interface Science, 2023, 318: 102960.

[21] Li Z X, Yang W, Chen Z, et al. Boron nitride- and carbon nanotube-bridged interfaces for boosting thermal conduction and electromagnetic wave absorption[J]. ACS Applied Nano Materials, 2024, 7: 4264-4276.

[22] Jiang B, Yang W, Bai H X, et al. Facile fabrication of Fe/Fe_5C_2@N-doped porous carbon as an efficient microwave absorbent with strong and broadband absorption properties at an ultralow filler loading[J]. Carbon, 2022, 196: 890-901.

[23] Li B, Tian H Y, Li L, et al. Graphene assisted assembly of electrically and magnetically conductive ceramic nanofibrous zerogels enable multifunctionality[J]. Advanced Functional Materials, 2024, 34: 2314653.

[24] Gao T, Rong H, Mahmoud K H, et al. Iron/silicon carbide composites with tunable high-frequency magnetic and dielectric properties for potential electromagnetic wave absorption[J]. Advanced Composites and Hybrid Materials, 2022, 5: 1158-1167.

[25] Wang L H, Su S L, Wang Y D. Fe_3O_4-Graphite composites as a microwave absorberwith bimodal microwave absorption[J]. ACS Applied Nano Materials, 2022, 5: 17565-17575.

[26] Pan J J, Xia W, Sun X, et al. Improvement of interfacial polarization and impedance matching for two-dimensional leaf-like bimetallic (Co, Zn) doped porous carbon nanocomposites with broadband microwave absorption[J]. Applied Surface Science, 2020, 512: 144894.

[27] Song F Y, Zhang Z C, Li W, et al. Direct growth of edge-rich graphene with tunable dielectric properties in porous Si_3N_4 ceramic for broadband high-performance microwave absorption[J]. Advanced Functional Materials, 2018, 28: 1707205.

[28] Liang L L, Song G, Liu Z, et al. Constructing $Ni_{12}P_5$/Ni_2P heterostructures to boost interfacial polarization for enhanced microwave absorption performance[J]. ACS applied materials & interfaces, 2020, 12: 52208-52220.

[29] Jiang B, Yang W, Bai H X, et al. Multiscale structure and interface engineering of Fe/Fe_3C in situ encapsulated in nitrogen-doped carbon for stable and efficient multi-band electromagnetic wave absorption[J]. Journal of Materials Science & Technology, 2023, 158: 9-20.

[30] Liu D W, Yang L, Wang F Y, et al. Hierarchical carbon nanotubes@Ni/C foams for high-performance microwave absorption[J]. Carbon, 2022, 196: 867-876.

[31] Di X C, Wang Y, Lu Z, et al. Heterostructure design of Ni/C/porous carbon nanosheet composite for enhancing the electromagnetic wave Absorption[J]. Carbon, 2021, 179: 566-578.

[32] Zhang X, Yan F, Zhang S, et al. Hollow N-doped carbon polyhedron containing CoNi alloy nanoparticles embedded within fewlayer N-doped graphene as high-performance electromagnetic wave absorbing material[J]. ACS applied materials & interfaces, 2018, 10: 24920-24929.

[33] Wang C X, Liu Y, Jia Z R, et al. Multicomponent nanoparticles synergistic one-dimensional nanofibers as heterostructure absorbers for tunable and efficient microwave absorption[J]. Nano-micro Letters, 2023, 15: 16.

[34] Gong X B, Liu Q L, Zhao W, et al. Almond C/Fe_xO_y composite material based on biomass porous carbon structure with high-efficiency microwave absorbing properties[J]. Journal of Materials Science-materials in Electronics, 2022, 33: 13166-13179.

[35] Du B Y, Zhu H W, Xu J Y, et al. N-S co-doping lignin-based carbon magnetic nanoparticles as high performance supercapacitor and electromagnetic wave absorber[J]. International Journal of Biological Macromolecules, 2023, 242: 125032.

[36] Qiu Y, Lin Y, Yang H B, et al. Hollow Ni/C microspheres derived from Ni-metal organic framework for electromagnetic wave absorption[J]. Chemical Engineering Journal, 2020, 383: 123207.

[37] Liu Z L, Su S L, Zhao Y M, et al. Multi-morphology composite: Particle & petal-shaped $ZnFe_2O_4$/flower-shaped ZnO@Porous biomass carbon with excellent broadband microwave absorption performance[J]. Carbon, 2023, 215: 118448.

[38] Wang Y C, Li W Y, Li H M, et al. Fe/Fe_3C@CNTs anchored on carbonized wood as both self-standing anode and cathode for synergistic electro-Fenton oxidation and sequestration of As(III)[J]. Chemical Engineering Journal, 2021, 414: 128925.

[39] Cheng J B, Zhao H B, Zhang A N, et al. Porous carbon/Fe composites from waste fabric for high-efficiency electromagnetic wave absorption[J]. Journal of Materials Science Technol, 2022, 126: 266-274.

[40] Wu P K, Chen T, Liu C Y, et al. Confinement engineering to enhance broadband microwave absorption of hierarchically magnetic carbon tubular composite[J]. Carbon, 2023, 214: 118353.

[41] Li Q S, Liu Q C, Kong X K. Noncovalent heterointerface on boron-carbon hybrid for improved microwave absorption[J]. Journal Of Materials Science, 2020, 55: 14345-14357.

[42] Huang F, Wang S, Ding W, et al. Sulfur-doped biomass-derived hollow carbon microtubes toward excellent microwave absorption performance[J]. Journal of Materials Science: Materials in Electronics, 2021, 32: 6260-6268.

[43] Guo R D, Su D, Chen F, et al. Hollow beaded Fe_3C/N-doped carbon fibers toward broadband microwave absorption[J]. ACS Applied Materials & Interfaces, 2022, 14: 3084-3094.

[44] Cheng J B, Liu B W, Wang Y Q, et al. Growing CoNi nanoalloy@N-doped carbon nanotubes on MXene sheets for excellent microwave absorption[J]. Journal Of Materials Science& Technology, 2022, 130: 157-165.

[45] Gang H Y, Deng H Y, Yan L J, et al. Surface redox pseudocapacitance boosting Fe/Fe_3C nanoparticles-encapsulated N-doped graphene-like carbon for high- performance capacitive deionization[J]. Journal Of Colloid And Interface Science, 2023, 638: 252-262.

[46] Chen Y, Qiang R, Shao Y L, et al. Biomass-derived Fe/C composites for broadband electromagnetic wave response[J]. Journal Of Alloys And Compounds, 2023, 968: 171952.

[47] Xu Y, Chen S, Ye M F, et al. Fe/Fe_3C anchored on activated N-doped porous carbon for sensitive and selective determination of levodopa[J]. Microchemical Journal, 2025, 212: 113504.

[48] Gao S S, An Q D, Xiao Z Y, et al. Controllable N-doped carbonaceous composites with highly dispersed Ni nanoparticles for excellent microwave absorption[J]. ACS Applied Nano Materials, 2018, 1(10): 5895-5906.

[49] Lin X X, Zhou Y H, Hong J F, et al. Facile preparation of ZIF-8/ZIF-67-derived biomass carbon composites for highly efficient electromagnetic wave absorption[J]. Chinese Chemical Letters, 2024, 35: 109835.

[50] Du H Y, Jiang J, Ren L J, et al. Fe_3C/Fe@N-doped porous carbon composites with excellent microwave absorption properties[J]. Colloids and Surfaces A: Physico- chemical and Engineering Aspects, 2023, 670: 131564.

[51] Liang J, Ye F, Cao Y, et al. Defect-engineered grapheme/Si_3N_4 multilayer alternating core-shell nanowire membrane: a plainified hybrid for broadband electromagnetic wave absorption[J]. Advanced Functional Materials, 2022, 32: 2200141.

[52] Wei B, Zhou C Y, Yao Z J, et al. Lightweight and high efficiency microwave absorption of reduced graphene oxide loaded with irregular agnetic quantum dots[J]. Journal Of Alloys And Compounds, 2021, 886: 161330.

[53] Zhao Y Z , Wang W, Wang Q J, et al. Construction of excellent electromagnetic wave absorber from multi-heterostructure materials derived from $ZnCo_2O_4$ and ZIF-67 composite[J]. Carbon, 2021, 185: 514-525.

[54] Wu Z C, Pei K, Xing L S, et al. Enhanced microwave absorption performance from magnetic coupling of magnetic nanoparticles suspended within hierarchically tubular composite[J]. Advanced Functional Materials, 2019, 1901448.

[55] Zhang Y F, Li Y L, Wei M M, et al. Core- shell structured Co@NC@MoS_2 magnetic hierarchical nanotubes: preparation and microwave absorbing properties[J]. Journal of Materials Science & Technology, 2022, 128: 148-159.

[56] Liu P B, Gao S, Zhang G Z, et al. Hollow Engineering to Co@N-doped carbon nanocages via synergistic protecting-etching strategy for ultrahigh microwave absorption[J]. Advanced Functional Materials, 2022, 31: 2102812.

[57] Quan B, Shi W, Hong S J, et al. Defect engineering in two common types of dielectric materials for electromagnetic absorption applications[J]. Advanced Functional Materials, 2019, 29: 1901236.

[58] Qiu J, Liao J, Wang G, et al. Implanting N-doped CQDs into rGO aerogels with diversified applications in microwave absorption and wastewater treatment[J]. Chemical Engineering Journal, 2022, 443: 136475.

[59] Zhang X C, Shi Y N, Xu J, et al. Identification of the intrinsic dielectric properties of metal single atoms for electromagnetic wave absorption[J]. Nano-Micro Letters, 2021, 14: 27.

[60] Yao C, Wu Z H, Liu J Y, et al. Construction of lychee-like MoS_2 microspheres on rice husk-derived porous carbon for enhanced dielectric loss and efficient electromagnetic wave absorption[J]. Journal Of Materials Science-materials In Electronics, 2023, 34: 1213.

[61] Xia Y X, Gao W W, Gao C, et al. A review on graphene-based electromagnetic functional materials: electromagnetic wave shielding and absorption[J]. Advanced Functional Materials, 2022, 32: 2204591.

[62] Zhang X, Qiao J, Wu N, et al. Conductive bimeta-organic frameworks with volcano-type fine-tuned dielectric properties for electromagnetic wave absorption[J]. American Chemical Society Nano, 2025, 19: 26761-26769.

[63] Li Z X, Yang W, Jiang B, et al. Engineering of the core-shell boron nitride@ nitrogen-doped carbon heterogeneous interface for efficient heat dissipation and electromagnetic wave absorption[J]. ACS Applied Materials & Interfaces, 2023, 15: 7578-7591.

[64] Qiao J, Song Q H, Xuan L X, et al. Dual cross-linked magnetic MXene aerogel with high strength and durability enables multifunctionality[J]. Advanced Functional Materials, 2024, 34: 2401687.

[65] Ning T G, Li Q Y, Ren Q Q, et al. Kapok fibers-derived carbon microtubes as efficient electromagnetic wave absorption materials[J]. Ceramics International, 2023, 49: 29339-29347.

[66] Ji C, Liu Y, Xu J, et al. Enhanced microwave absorption properties of biomass-derived carbon decorated with transition metal alloy at improved graphitization degree[J]. Journal Of Alloys And Compounds, 2021, 890: 161834.

[67] Shi J, Zhang X, He W J, et al. Biomass-derived porous carbon materials for tunable microwave absorption with excellent low-frequency performance[J]. ACS Applied Materials & Interfaces, 2025, 17: 39440-39447.

[68] Lu C X, Zhao J Q, An Z J, et al. Biomass-derived spherical carbon materials for efffcient electromagnetic wave absorption[J]. ACS Applied Materials & Interfaces, 2024, 6: 7623-7632.

[69] Yi Q J, Li C L, Zhang F, et al. Carbon nanotube grown from cobalt supported on biomass-derived carbon as nanocomposite for the attenuation of electromagnetic waves[J]. ACS Applied Nano Materials, 2024, 7: 23763-23776.

[70] Wu Z H, Yao C, Meng Z Z, et al. Biomass-derived crocodile skin-like porous carbon for high-performance microwave absorption[J]. Advanced Sustainable Systems, 2022, 6: 2100454.

[71] Yang B T, Fang J F, Xu C Y, et al. One-dimensional magnetic FeCoNi alloy toward low-frequency electromagnetic wave absorption[J]. Nano-Micro Letters, 2022, 14: 170.

[72] Chen J X, Chen P Q, Li X C, et al. Enhancement of electromagnetic attenuation of network CNT-carbon microsphere nanocomposites derived from phenolic resin[J]. Carbon, 2024, 219: 118789.

[73] Wu P K, Kong X K, Feng Y R, et al. Phase engineering on amorphous/crystalline γ-Fe_2O_3 nanosheets for boosting dielectric loss and high-performance microwave absorption[J]. Advanced Functional Materials, 2024, 34: 2311983.

[74] Wu Z C, Pei K, Xing L S, et al. Enhanced microwave absorption performance from magnetic coupling of magnetic nanoparticles suspended within hierarchically tubular composite[J]. Advanced Functional Materials, 2019, 29(28): 1901448.

[75] Wu P k, Feng Y R, Xu J, et al. Ultralight N-doped platanus acerifolia biomass carbon microtubes/RGO composite aerogel with enhanced mechanical properties and high-performance microwave absorption[J]. Carbon, 2023, 202: 194-203.

[76] Wu F, Xie A, Jiang L, et al. Inorganic–organic hybrid dielectrics for energy conversion: mechanism, Strategy, and Applications[J]. Advanced Functional Materials, 2023, 33(28): 2212861.